

Optical investigations of quantum dot spin dynamics as a function of external electric and magnetic fields

Jan Dreiser, Mete Atatüre, Christophe Galland, Tina Müller, Antonio Badolato, and Atac Imamoglu
Institute of Quantum Electronics, ETH Zürich, Wolfgang-Pauli-Strasse, CH-8093 Zürich, Switzerland

(Received 24 May 2007; published 19 February 2008)

We have performed all-optical measurements of spin relaxation in single self-assembled InAs/GaAs quantum dots (QDs) as a function of static external electric and magnetic fields. To study QD spin dynamics, we measure the degree of resonant absorption which results from a competition between optical spin pumping induced by the resonant laser field and spin relaxation induced by reservoirs. Fundamental interactions that determine spin dynamics in QDs are hyperfine coupling to QD nuclear spin ensembles, spin-phonon coupling, and exchange-type interactions with a nearby Fermi sea of electrons. We show that the strength of spin relaxation generated by the three fundamental interactions can be changed by up to 5 orders of magnitude upon varying the applied electric and magnetic fields. We find that the strength of optical spin pumping that we use to study the spin relaxation is determined predominantly by hyperfine-induced mixing of single-electron spin states at low magnetic fields and heavy-light hole mixing at high magnetic fields. Our measurements allow us to determine the rms value of the hyperfine (Overhauser) field to be ~ 15 mT with an electron g factor of $g_e=0.6$ and a hole mixing strength of $|\epsilon_H|^2=5 \times 10^{-4}$.

DOI: [10.1103/PhysRevB.77.075317](https://doi.org/10.1103/PhysRevB.77.075317)

PACS number(s): 78.67.Hc, 72.25.Rb, 71.35.Pq, 71.70.Jp

I. INTRODUCTION

A single quantum dot (QD) electron spin is a fundamental physical system which allows for a controlled study of confined spin dynamics in the solid state. In contrast to higher-dimensional semiconductor structures, QD spins can possess long relaxation and coherence times exceeding 20 ms and 10 μ s, respectively. The prolongation of spin relaxation times for QD spins stems from a drastic reduction in spin-phonon coupling mediated by a combination of electron-phonon and spin-orbit interactions, due to strong quantum confinement of electrons. As a consequence, additional spin-reservoir interactions such as hyperfine coupling to QD nuclear spins and exchange-type (cotunneling) coupling to a nearby Fermi sea become prominent in determining the spin dynamics in QDs, providing an interestingly rich physical system to study.

Major advances in understanding relaxation and coherence of single confined electron spins have been made primarily in electrically defined QDs: Spin lifetimes of ~ 1 ms at high magnetic fields¹ (8 T) and up to an impressive 170 ms low magnetic fields² (1.75 T) have been recently observed. Rabi oscillations using microwave pulses³ confirmed the long coherence times for electron spins. In coupled QDs, hyperfine-induced singlet-triplet mixing,⁴ relaxation,⁵ and coherence⁶ have been studied. On the self-assembled QD front, optical measurements on InAs/GaAs self-assembled QD ensembles have revealed T_1 times exceeding 20 ms at a magnetic field of 4 T and a temperature of 1 K.⁷ These findings overall have strengthened the initial proposals for utilizing optical and/or electrical control over QD spins, which act as physical representation of qubits in quantum information processing.^{8–10}

Here, we present a complete experimental and theoretical study of the dynamics of an electron spin confined in a self-assembled InAs/GaAs QD which is, in turn, embedded in a Schottky heterostructure. In a nutshell, we are able to show

the interplay of all interactions present in a single QD for the largest parameter range reported to date. We measure the degree of resonant absorption to assess the relative importance and external field dependence of the three elementary spin-relaxation mechanisms, since it is determined by the competition between optical spin pumping¹¹ (OSP) and reservoir-induced spin relaxation. Using numerical calculations based on our theoretical model, we are able to obtain an excellent fit to our experimental data.

First, we show that at low magnetic fields (up to 1 T), hyperfine interaction shoulders an unexpected dual role, where it alone acts both as a mediator for relaxing (heating) and pumping (cooling) the electron spin in the presence of a resonant laser field. We demonstrate that spontaneous spin-flip Raman scattering that allows for one-way pumping into the optically uncoupled spin state is predominantly enabled by a mixing between the electronic spin states induced by the transverse component of the fluctuating nuclear (Overhauser) field. Further, we find that the quasistatic approximation^{12,13} for nuclear spins is sufficient to explain our experimental results due to the long correlation times of the nuclear spins themselves and to break down the validity of a standard reservoir assumption for nuclear spins. Next, we show that upon varying the external gate voltage by about 50 mV, the spin relaxation due to exchange coupling to the nearby Fermi sea of electrons can be changed by as much as 5 orders of magnitude. Finally, we show that in the high-magnetic-field regime (2–10 T), spin pumping is due to heavy-light hole mixing and spin relaxation is dominated by phonons in conjunction with spin-orbit interaction.

This paper is organized as follows: In Sec. II, we present a theoretical model that describes the QD spin dynamics in the framework of the trion four-level system with spin-reservoir coupling. Experimental results obtained with single QD absorption spectroscopy in distinct regimes of external electric and magnetic fields where different interactions dominate are discussed in Sec. III. Finally, Sec. IV gives an

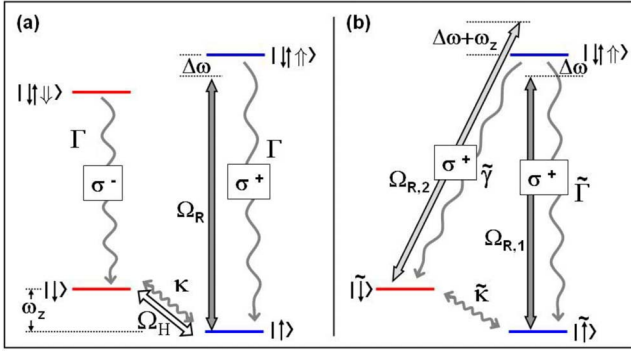


FIG. 1. (Color online) (a) Four-level system describing the singly charged QD in magnetic field along the growth direction (z axis). The electronic ground states with Zeeman splitting $\hbar\omega_z$ are vertically coupled by circularly polarized optical transitions to excitonic (trion) states. These consist of a heavy hole and two electrons forming a singlet. The fluctuations of the hyperfine field lead to a slowly varying coherent coupling $\Omega_H = \Omega_H(t)$ of the spin ground states. Incoherent spin-flip processes due to cotunneling and phonon-SO coupling are taken into account by relaxation rate κ . A laser is introduced at Rabi frequency Ω_R and detuning $\Delta\omega$ from the trion transition. (b) Transformed system after elimination of coherent coupling Ω_H ; this system is physically equivalent to that shown in (a). A weak hyperfine-induced diagonal transition appears at rate $\tilde{\gamma} \propto \Omega_H^2/B_z^2$. The laser is now detuned on the weak $\tilde{\gamma}$ transition with a reduced Rabi frequency $\Omega_{R,2}$.

overview on the above-mentioned interactions together in a self-contained picture. Appendixes are provided at the end for further details and technicalities such as sample structure and experimental techniques for those interested.

II. GROUND-STATE OPTICAL TRANSITIONS OF THE SINGLY CHARGED DOT

A singly charged QD is described as a four-level system with two ground states and two excited states, coupled by two vertical optical transitions, as shown in Fig. 1(a). The ground state $|\uparrow\rangle$ ($|\downarrow\rangle$) with angular momentum projection $m_z = +1/2$ ($m_z = -1/2$) is coupled to an excited state (trion state) formed out of two electrons in a singlet and a heavy hole $|\downarrow\uparrow\uparrow\rangle$ ($|\downarrow\uparrow\downarrow\rangle$) with spin projection $m_z = +3/2$ ($m_z = -3/2$). The optical transitions with spontaneous emission rate Γ are σ^+ (σ^-) polarized according to optical selection rules. The states are defined as

$$\begin{aligned} |\uparrow\rangle &= e_{QD,+1/2}^\dagger |0\rangle, \\ |\downarrow\rangle &= e_{QD,-1/2}^\dagger |0\rangle, \\ |\uparrow\uparrow\rangle &= h_{QD,+3/2}^\dagger |0\rangle, \\ |\downarrow\uparrow\uparrow\rangle &= e_{QD,-1/2}^\dagger e_{QD,+1/2}^\dagger h_{QD,+3/2}^\dagger |0\rangle, \end{aligned} \quad (1)$$

where $e_{QD,\sigma}^\dagger$ ($h_{QD,\sigma}^\dagger$) is the operator that creates an electron (hole) in the QD with spin σ along the z axis, and $|0\rangle$ is the vacuum (empty dot) state.

All four states undergo different Zeeman shifts when an external dc magnetic field along the z axis is applied, leading to Zeeman splitting of the optical transitions. A σ^+ polarized laser field is introduced at Rabi frequency Ω_R and detuning $\Delta\omega = \omega_0 - \omega_L$, with ω_0 the frequency of the trion transition and ω_L the laser frequency. If only a σ^+ polarized laser field is present, the trion state with $m_z = -3/2$, i.e., ($|\downarrow\uparrow\downarrow\rangle$) is inactive since the coupling strength is reduced by a factor exceeding 10^3 at magnetic fields larger than 60 mT, due to a combination of selection rules and, in the presence of a magnetic field, optical detuning.¹⁴ As we shall discuss shortly, the weak spontaneous emission to the other spin ground state cannot be neglected due to its long lifetime. Thus, the system reduces to three levels.

The total Hamiltonian describing the system is

$$\hat{H} = \hat{H}_{\text{hyp}} + \hat{H}_{\text{charge}} + \hat{H}_{\text{phonon}} + \hat{H}_{\text{int,rad}} + \hat{H}_{\text{Zeeman}}. \quad (2)$$

The first three terms describe couplings to nuclear spin, free-electron gas, and phonon reservoirs, respectively. Details about these spin-reservoir couplings can be found in Appendix A. The interaction with the radiation field in semiclassical form can be expressed as $\hat{H}_{\text{int,rad}} = \hbar\Omega_R (e^{i\Delta\omega t} e_{QD,-1/2}^\dagger h_{QD,+3/2}^\dagger + \text{H.c.})$. The last term describes the Zeeman effect due to an external magnetic field.

A. Density matrix description of the quantum dot spin

In what follows, we treat hyperfine interactions via a random quasistatic field and the effect of exchange interactions with the Fermi gas and spin-phonon coupling as dissipative processes with rates described with a Born-Markov approximation. The dynamics of the system is then described using density matrix equations with an effective spin-Hamiltonian and dissipative terms in the Lindblad term.

The external magnetic field is aligned with the z axis $\mathbf{B}_{\text{ext}} = \mathbf{B}_z = (0, 0, B_z)$. The total magnetic field at the QD is $\mathbf{B} = \mathbf{B}_z + \mathbf{B}_N$, where the nuclear magnetic field (second term) is only seen by the electron spin, but not the hole spin. Taking the sum of the hyperfine and Zeeman terms yields $\hat{H}_{\text{hyp}} + \hat{H}_{\text{Zeeman}} = \hbar\Omega_H(t)\hat{\sigma}_x + \hbar\omega_z\hat{\sigma}_z + g_h\mu_B B_z \cdot \hat{J}_z$, with $\Omega_H(t)$ as defined in Eq. (A4). $\hat{\sigma}_i$ are the Pauli matrices, g_h is the QD hole g factor, μ_B is the Bohr magneton, and \hat{J}_z is the z component of the hole spin operator. In addition, $\hbar\omega_z = g_e\mu_B[B_z + B_{N,z}(t)]$, with g_e the QD electron g factor. Using the notation $|1\rangle = |\downarrow\rangle$, $|2\rangle = |\uparrow\rangle$, and $|3\rangle = |\downarrow\uparrow\uparrow\rangle$, the unitary part of the Hamiltonian can be written as

$$\hat{H}_0 = \hbar \begin{pmatrix} \omega_z & \Omega_H(t) & 0 \\ \Omega_H(t) & 0 & \Omega_R \\ 0 & \Omega_R & \omega_0 - \omega_L \end{pmatrix}. \quad (3)$$

The time evolution of $\Omega_H(t)$ is much slower than all the time scales over which the system reaches steady state. Therefore, $\Omega_H(t) \approx \Omega_H$ is a valid substitution for such a quasistatic system.

Each spin-reservoir coupling is included in our three-level model as an incoherent relaxation rate κ_i coupling states $|1\rangle \leftrightarrow |2\rangle$ bidirectionally. Each κ_i depends on external mag-

netic and/or electric field. The coupling of the trion states due to hole spin relaxation has been neglected here due to the low probability of the system being in the excited state manifold. This issue is discussed in Sec. III G. The total spin relaxation rate is

$$\kappa = \sum \kappa_i = f(V_g, B_z) = \kappa_{\text{cotunnel}}(V_g, B_z) + \kappa_{\text{phonon}}(B_z) + \kappa_{\text{exp}}. \quad (4)$$

Here, V_g is the gate voltage and κ_{exp} describes an experimentally induced spin-relaxation rate. Under normal conditions, this relaxation is absent, but can be invoked by large-amplitude gate-voltage modulation in electron cycling experiments as discussed in Sec. III.

The explicit three-level Bloch equations are derived in Appendix C for completeness.

B. Dressed states and rate equation description of spin pumping

In the following, we will transform the system into another basis that gives an intuitive picture and we will see that optical coupling of the three levels forms a Λ system. This allows us to capture the main features of the spin dynamics in the form of rate equations.

The new basis states that diagonalize the 2×2 ground spin-state subset of the Hamiltonian of Eq. (3) is $|\tilde{1}\rangle = |\tilde{1}\rangle = \cos \phi |1\rangle - \sin \phi |2\rangle$, $|\tilde{\uparrow}\rangle = |\tilde{2}\rangle = \sin \phi |1\rangle + \cos \phi |2\rangle$, and $|\downarrow \tilde{\uparrow}\rangle = |\tilde{3}\rangle = |3\rangle$, with $\phi = \Omega_H / \omega_z$. Based on the experimental regimes studied here, we can simplify the calculations since $\phi \ll 1$ typically and only take into account first-order terms in ϕ . Appendix D addresses this step in more detail. The transformed Hamiltonian then is

$$\tilde{H}_0 = \hbar \begin{pmatrix} \omega_z & 0 & \Omega_{R,1} \\ 0 & 0 & \Omega_{R,2} \\ \Omega_{R,1} & \Omega_{R,2} & \Delta\omega \end{pmatrix}. \quad (5)$$

The off-diagonal terms due to Ω_H have been eliminated, and it becomes clear that both ground states couple to the excited state via an optical transition. Also the spontaneous emission terms become modified into a strong and a weak channel, marked by spontaneous emission rates $\tilde{\Gamma}$ and $\tilde{\gamma}$.

The result of the transformation is shown in Fig. 1(b): A single laser that interacted with the σ^+ trion transition is now represented by two laser field coupling states $|\tilde{1}\rangle$ and $|\tilde{3}\rangle$ ($|\tilde{2}\rangle$ and $|\tilde{3}\rangle$, respectively). Effectively, the system can be decomposed into two two-level systems with their own spontaneous emission rates, Rabi frequencies, and effective laser detunings. Those are for the $|\tilde{1}\rangle \leftrightarrow |\tilde{3}\rangle$ subsystem:

$$\tilde{\gamma} = \phi^2 \Gamma, \quad \tilde{\Omega}_{R,1} = \phi \Omega_R, \quad \tilde{\Delta}\omega_1 = \Delta\omega + \omega_z, \quad (6)$$

and for the $|\tilde{2}\rangle \leftrightarrow |\tilde{3}\rangle$ subsystem:

$$\tilde{\Gamma} = \Gamma, \quad \tilde{\Omega}_{R,2} = \Omega_R, \quad \tilde{\Delta}\omega_2 = \Delta\omega. \quad (7)$$

In the following, we will discuss the properties of the transformed three-level system with a resonant laser on the

$|\tilde{2}\rangle \leftrightarrow |\tilde{3}\rangle$ subsystem. We start out with the system being in state $|\tilde{2}\rangle$. After an intermediate time t_0 given by $\tilde{\gamma}^{-1} \gg t_0 \gg \Gamma^{-1}$, the laser field induces a steady-state occupation of the excited state $\tilde{\rho}_{33}(t_0)$. Here, $\tilde{\rho}_{ij}$ denotes the element in row i and column j of the transformed systems' density operator. Further, for times much longer than $[\tilde{\rho}_{33}(t_0) \tilde{\gamma}]^{-1}$, the system can also be found in state $|\tilde{1}\rangle$. The net effect of this spin-flip Raman process is a transfer of occupation from state $|\tilde{2}\rangle$ to state $|\tilde{1}\rangle$. We will refer to this process as OSP, due to its similarity to experiments performed with atoms.¹⁵ Further, we note that a scheme that uses OSP for spin-state preparation had been proposed in Ref. 16

In order to obtain the transfer rate from state $|\tilde{2}\rangle$ to state $|\tilde{1}\rangle$, and vice versa, under the presence of a resonant laser ($\Delta\omega=0$), we apply rate equation approximations as discussed in, e.g., Ref. 17. We obtain $R_{2 \rightarrow 1} = \frac{\Omega_{R,2}^2}{\tilde{\Gamma}^2 + 2\Omega_{R,2}^2} \tilde{\gamma}$ and $R_{1 \rightarrow 2} = \frac{\Omega_{R,1}^2 \tilde{\Gamma}}{4\omega_z^2 + \tilde{\Gamma}^2} \approx \frac{\Omega_{R,1}^2 \tilde{\Gamma}}{4\omega_z^2}$. Under the conditions of $\kappa \ll R_{1 \rightarrow 2}$, $R_{2 \rightarrow 1}$, weak incident beam ($\Omega_R \ll \tilde{\Gamma}$), and a Zeeman splitting largely exceeding the trion decay rate ($\omega_z \gg \tilde{\Gamma}$), we have

$$\tilde{\rho}_{22}(t = \infty) \approx \frac{1}{1 + \frac{4\omega_z^2}{\tilde{\Gamma}^2}}. \quad (8)$$

In the case $R_{1 \rightarrow 2} \ll \kappa$, $R_{2 \rightarrow 1}$,

$$\tilde{\rho}_{22}(t = \infty) \approx \frac{1}{2 + \zeta}, \quad \zeta = \frac{\tilde{\gamma}}{\kappa} \frac{\Omega_R^2}{\tilde{\Gamma}^2 + 2\Omega_R^2}. \quad (9)$$

Hence, in the case of fixed laser intensity, i.e., constant Ω_R^2 , the spin-state occupations are determined by the ratio of OSP rate versus spin-relaxation rate.

C. Hole mixing

Valence-band mixing, as described by the Luttinger Hamiltonian,¹⁸ is a well-known feature in quantum wells. Although being dramatically reduced, it is, nevertheless, expected to play a role in quantum dot dynamics. With valence-band mixing, a heavy hole acquires a small contribution of light holes, and vice versa, such that the effective hole state as it was defined in Eq. (1) has the form $|\uparrow\rangle_{\text{hmix}} = (h_{QD,+3/2}^\dagger + \epsilon_{H_+} h_{QD,+1/2}^\dagger + \epsilon_{H_-} h_{QD,-1/2}^\dagger) |0\rangle$ with $|\epsilon_{H_\pm}| \ll 1$. Pseudopotential calculations for self-assembled InAs QDs yield admixtures on the order of a few percent.¹⁹ As it has been pointed out in Ref. 10, valence-band mixing would have a major impact on the effective optical selection rules by introducing a diagonal relaxation channel between states $|3\rangle$ and $|1\rangle$ due to the admixed light hole component of state $|3\rangle$. Two cases have to be distinguished: First, the mixing contribution associated with ϵ_{H_+} further leads to an effective coherent laser coupling in addition to the coupling induced by hyperfine interaction ($\propto \frac{\Omega_H}{\omega_z} \Omega_R$) at a detuning $\Delta\omega + \omega_z$ as shown in Fig. 1(b). Second, the ϵ_{H_-} part essentially only appears as a relaxation channel without coherent laser coupling, as the dipole mo-

ment of this linearly polarized transition lies along the propagation axis of the laser beam and, therefore, cannot be excited. Hence, the following diagonal relaxation terms are added to Eq. (C1),²⁰ $\hat{L}_{\text{relax, hm}} = \frac{\gamma_{\text{hm}}}{2}(2\hat{\sigma}_{13}\hat{\rho}\hat{\sigma}_{31} - \hat{\sigma}_{33}\hat{\rho} - \hat{\rho}\hat{\sigma}_{33})$ with $\gamma_{\text{hm}} = |\epsilon_H|^2\Gamma = (|\epsilon_{H_+}|^2 + |\epsilon_{H_-}|^2)\Gamma$.

This diagonal rate leads to OSP in a way similar to the $\tilde{\gamma}$ channel enabled by hyperfine interaction. The main difference between hyperfine-induced OSP and valence-band mixing induced OSP is that the first one is magnetic-field dependent as discussed previously, and the latter is not: the valence-band mixing strength ϵ_H is expected to be independent of magnetic field as long as the Zeeman splitting is much smaller than the heavy-light hole splitting ($\Delta_{hl} > 10$ meV), which is true for all realistic experimental magnetic fields. Since the hyperfine-induced OSP rate drops with magnetic field $\tilde{\gamma} \propto B_z^{-2}$, hole-mixing-induced OSP should dominate at high fields. From our measurements at high magnetic fields [Fig. 7(b)], we extract a γ_{hm}^{-1} of $2 \pm 0.8 \mu\text{s}$, which yields a hole-mixing strength of $|\epsilon_H| \sim 2.2\%$. This $|\epsilon_H|$ value is, indeed, much smaller than 1, in agreement with previous theoretical studies.

Before closing this section of theoretical considerations, we note that a slightly tilted external magnetic field would yield identical dynamics in the absence of any hole mixing since it would lead to mixing of electronic states induced by the in-plane component of the applied field. These two fundamentally different mechanisms are experimentally indistinguishable for a fixed magnetic-field orientation. Therefore, we repeated our experiments as a function of sample tilt under a magnetic field. For a $\pm 1.5^\circ$ coverage of tilt in all directions, our measurements yielded no observable change in the measured quantity γ_{hm} . Hence, we can safely state that the inherent hole mixing in our QDs, indeed, dominates over small-angle tilt-induced mixing of electronic spin states.

III. SINGLE DOT ABSORPTION SPECTROSCOPY WITH RESONANT LASER

A. Experimental method

All data shown in this work have been obtained using differential transmission (DT) technique.^{21–26} Details regarding our sample and experiment can be found in Appendix B. In order to link the experimentally observable absorption to the three-level system of the singly charged QD, we use the effective Λ -system picture as described in the previous section. With a resonant laser and large external magnetic field along the z axis, i.e., $\Delta\omega = 0$, $\omega_z \gg \tilde{\Gamma} \gg \tilde{\gamma}$, the $\tilde{2} \leftrightarrow \tilde{3}$ subsystem with strong spontaneous emission rate $\tilde{\Gamma}$ acts as the main scattering source.

The QD response in this type of DT experiments is discussed in the above-mentioned references. In the following, we, therefore, only sketch the link between our three-level system and the intensity of the light transmitted through the sample. The signal detected in a DT experiment arises from interference of the forward scattered field together with the excitation field. This can also be seen from the optical theorem²⁷ which relates the *absorption* cross section of the dipole to the forward-scattering amplitude. When the QD is

exactly at the focus, the imaginary part of the scattered field is in phase with the excitation laser.

After collecting all factors describing spatial mismatch between excitation field and QD scattering cross section, we define relative absorption caused by the $|\tilde{2}\rangle \leftrightarrow |\tilde{3}\rangle$ optical transition as

$$\Theta(\Delta\omega) = 1 - \frac{T(\Delta\omega)}{T_{\text{off}}} = s \text{Im}\left(-\frac{\Gamma}{\Omega_R} \tilde{\rho}_{32}(\infty)\right), \quad (10)$$

where $T(\Delta\omega)$ refers to the transmitted intensity as a function of laser detuning and T_{off} to the transmitted intensity far off-resonance in the limit ($\Delta\omega \rightarrow \infty$). On resonance in the weak excitation regime, i.e., $\Omega_R \ll \Gamma$, the term $\text{Im}\left(\frac{\Gamma}{\Omega_R} \tilde{\rho}_{32}(\infty)\right)$ reaches 1 and s is a scaling factor characterizing the maximum theoretical absorption contrast that is given by $s = S_{\text{exp}} \frac{\sigma_0}{A_L}$ valid for a weak focusing geometry. Here, σ_0 is the scattering cross section of the two-level system in the weak excitation limit and A_L is the laser spot area. The factor S_{exp} accounts for reduction of signal due to our lock-in detection scheme and experimental imperfections. Further, with $\Delta\omega = 0$, $\tilde{\rho}_{32}(\infty) = -i \frac{\Gamma}{\Omega_R} \tilde{\rho}_{33}(\infty)$ and Eq. (10) becomes

$$\Theta(\Delta\omega = 0) = 1 - \frac{T(\Delta\omega = 0)}{T_{\text{off}}} = s \frac{\Gamma^2}{\Omega_R^2} \tilde{\rho}_{33}(\infty). \quad (11)$$

Using Eq. (11), we will infer the value of the spin-up state occupation $\tilde{\rho}_{22}(\infty)$ from our absorption measurements when varying parameters such as magnetic field and gate voltage but keeping laser power constant, i.e., constant Ω_R . We still need a calibration point, i.e., an experimental value of $\Theta(0)$ for a known $\tilde{\rho}_{22}(\infty)$. In the absence of an external magnetic field, the spin ground states can be considered to be fully mixed due to the in-plane part of the Overhauser field, leading to $\tilde{\gamma} \sim \tilde{\Gamma}$ and a branching ratio of $\eta = 1$. As a consequence, the $|\tilde{1}\rangle - |\tilde{3}\rangle$ and the $|\tilde{2}\rangle - |\tilde{3}\rangle$ transitions equally contribute to light scattering and fast bidirectional OSP takes place, leading to a fully randomized spin, i.e., $\tilde{\rho}_{11}(t = \infty, B_z = 0) = \tilde{\rho}_{22}(t = \infty, B_z = 0) = \frac{1}{2}$. That having said, expression (11) can be rewritten by introducing a factor s' which can then be experimentally determined

$$\Theta(\Delta\omega = 0) = 1 - \frac{T(\Delta\omega = 0)}{T_{\text{off}}} = s' \frac{\Gamma^2}{\Omega_R^2} \tilde{\rho}_{22}(\infty). \quad (12)$$

B. Optical spin pumping

Figure 2(a) shows absorption on resonance on the blue Zeeman transition as a function of magnetic field normalized to on-resonance absorption at 0 T, i.e., $\Theta(B_z)/\Theta(B_z=0)$. The gate voltage was kept in the plateau center, i.e., in a regime where $\kappa_{\text{cottonnel}}$ is minimal. The inset shows the corresponding raw laser scans for 0 T (top) to 300 mT (bottom). The zero positions of the probe laser detuning has been readjusted in the graphs to compensate the Zeeman splitting.

Absorption drops by nearly 2 orders of magnitude over the plotted range of $B_z = 0$ to 300 mT. With a resonant laser in the weak excitation limit and Zeeman splitting much

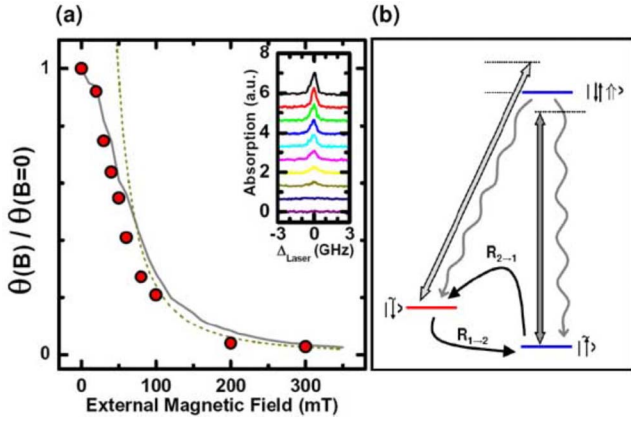


FIG. 2. (Color online) (a) Absorption maxima in the plateau center plotted as a function of magnetic field B_z . A drop occurs with increasing B_z due to OSP which, at low magnetic fields, dominates over cotunneling and phonon interaction. The gray line is a numerical simulation using $\Omega_R=0.6\Gamma$, $B_{\text{nuc}}=15$ mT, $\Gamma^{-1}=0.8$ ns, additional diagonal relaxation $\gamma_{hm}^{-1}=2$ μs , and $\kappa^{-1}=10$ ms. The inset shows the corresponding raw laser scans from 0 T (top) to 300 mT (bottom). The peaks have been shifted laterally to eliminate Zeeman splitting. (b) Optically induced spin pumping rates $R_{2\rightarrow 1}$, transferring the system into the dark state, and $R_{1\rightarrow 2}$ the back-pumping rate.

larger than the trion transition linewidth, i.e., $\Delta\omega=0$, and $\omega_z \gg \tilde{\Gamma} \gg \tilde{\gamma}$, Eq. (8) yielded $\tilde{\rho}_{22}(t=\infty) \approx 1/(1 + \frac{4\omega_z^2}{\tilde{\Gamma}^2})$ all provided that the spin-relaxation rate $\kappa \ll R_{2\rightarrow 1}, R_{1\rightarrow 2}$, which we can safely assume for low magnetic fields^{28,29} and strongly suppressed exchange coupling in the gate-voltage plateau center. Consistent with Eq. (8), the drop of absorption follows a $B^{-2} \propto \omega_z^{-2}$ law indicated by the dashed line. For fields less than 100 mT [see Fig. 2(a)], the approximations included in Eq. (8) do not hold anymore and $\tilde{\Gamma} \sim \tilde{\gamma}$. Without any approximation, the steady-state solutions of the optical Bloch equations are evaluated (solid line) numerically using a fluctuating Overhauser field; they are in excellent agreement with our data at all magnetic fields. The Rabi frequency Ω_R in units of Γ for a given incident laser power can be independently determined by saturation spectroscopy and power broadening measurements. The radiative lifetime $\Gamma^{-1}=0.8$ ns used in our simulation is based on a measurement in as-grown dots.³⁰

C. Electron cycling

Given that the OSP rates $R_{1\rightarrow 2}$, $R_{2\rightarrow 1}$ and the spin-relaxation rate κ are unknown, the experimental data shown in Fig. 2(a) do not reveal direct quantitative information about $\tilde{\gamma}$. However, the branching ratio η can be extracted using a rms-coherent coupling $\langle \Omega_H^2(t) \rangle$ given in Eq. (E1)

$$\eta = \frac{\tilde{\gamma}}{\tilde{\Gamma} + \tilde{\gamma}} = \frac{\langle \Omega_H^2(t) \rangle}{\omega_z^2} = \frac{B_{\text{nuc}}^2}{2B_z^2}. \quad (13)$$

η is equivalent to the probability that the system decays via the $\tilde{\gamma}$ channel when excited into a trion state.

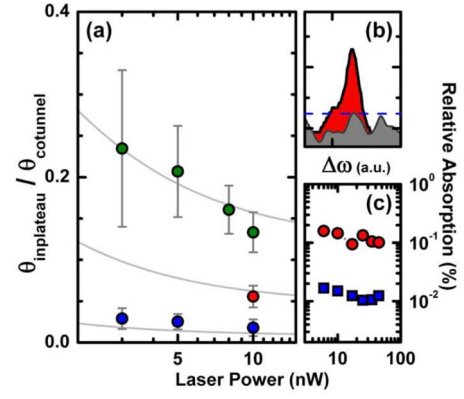


FIG. 3. (Color online) (a) Electron recycling measurements. Peak absorption in the plateau center normalized to peak absorption in the cotunneling regime is plotted as a function of laser power at a constant $B_z=300$ mT and three different $\kappa=\kappa_{\text{exp}}=54$ kHz (upper, green points), 19 kHz (middle, red points), and 3 kHz (lower, blue points). The fits indicated by the solid gray lines have been obtained using Eq. (9), yielding $\tilde{\gamma}_{\text{tot}}^{-1}=0.63$ μs . (b) A check experiment: Two laser scans at $\kappa=\kappa_{\text{exp}}=54$ kHz with in-and-out of plateau modulation (showing peak) and with in-plateau modulation, demonstrating that, indeed, controlled spin relaxation is realized. The noise level is indicated by the dashed blue line. (c) Intensity dependence of relative absorption at $B_z=0$ T (red circles) and $B_z=100$ mT (blue squares). There is essentially no dependence on laser power, confirming the theoretical model which gives Eq. (8).

To determine η , we applied a large square-wave modulation (amplitude of 80 mV peak to peak) at different frequencies to the gate which, in every cycle, first loaded another electron of opposite spin into the QD, forming a singlet together with the QD electron. Then one of the electrons was forced to leave, and as the tunneling probability for each of the two electrons is equal, the remaining QD spin was fully randomized. The advantage of this technique, which we will refer to as *electron cycling*, leads to enforced spin relaxation at a known and controlled rate κ_{exp} of Eq. (4). In the case $\kappa \approx \kappa_{\text{exp}} \gg R_{1\rightarrow 2}$, i.e., enforced spin-relaxation rate exceeds the optical back-pumping rate, $R_{2\rightarrow 1}$ and $\tilde{\gamma}$ can be determined by a fit using Eq. (9).

Figure 3(a) shows plateau-center absorption normalized to on-resonance absorption in the cotunneling regime; the data were obtained with electron cycling for different modulation frequencies and laser powers at a fixed external magnetic field $B_z=300$ mT. The upper, green points correspond to $\kappa=54.3$ kHz, the middle, red point to $\kappa=19.3$ kHz, and the lower, blue points to $\kappa=3.3$ kHz.

Using Eqs. (12) and (9), the absorption ratio shown in the figure can be written as

$$\frac{\theta_{\text{in-plateau}}}{\theta_{\text{cotunnel}}} = \frac{\rho_{22,\text{in-plateau}}}{\rho_{22,\text{cotunnel}}} = \frac{2}{2 + \zeta}. \quad (14)$$

The gray lines are fits using this expression. Best match with the data can be obtained with a total OSP rate $\gamma_{\text{tot}}(300 \text{ mT}) = \tilde{\gamma}(300 \text{ mT}) + \gamma_{hm} = 1.6$ μs^{-1} ,³¹ where the two contributions stem from nuclear spins and hole mixing, re-

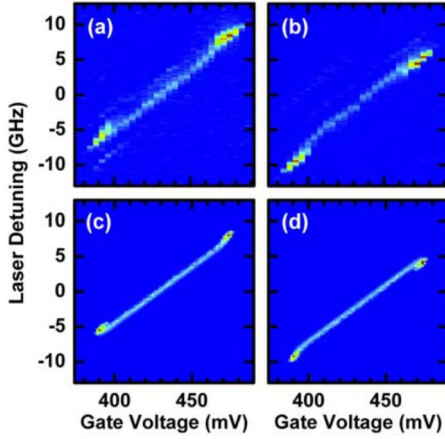


FIG. 4. (Color online) Absorption strength as a function of laser detuning and gate voltage. External magnetic field of $B_z=150$ mT is applied. The linear gate-voltage dependence is due to the quantum-confined Stark effect. (a) and (c) show the absorption in the vicinity of the blue optical transition, (b) and (d) show the red transition. (a) and (b) are experimental data showing a spectral shift of the weak absorption peak in the plateau center compared to the strong cotunneling regimes at the plateau edges. The shift is directed to the lower energies for the blue transition, and toward higher energies for the red transition. This feature can be reproduced in a numerical simulation including a randomly fluctuating Overhauser field as shown in (c) and (d) using the parameters $\Omega_R=0.6\Gamma$, $\Gamma^{-1}=0.8$ ns, $B_{\text{nuc}}=15$ mT, and $\gamma_{\text{hm}}^{-1}=2$ μs .

spectively. The hole mixing-induced contribution can be independently determined from high-magnetic-field measurements to be $\gamma_{\text{hm}}^{-1}=2$ μs . Using the branching ratio (13) with $\tilde{\Gamma}^{-1}=0.8$ ns, we then solve for the rms-nuclear magnetic field and obtain $B_{\text{nuc}}=15$ mT, which is in good agreement with the number obtained in Appendix A 1.

Figure 3(b) shows a measurement that demonstrates the difference between electron cycling (large-amplitude modulation) and in-plateau (small amplitude) modulation: For in-plateau modulation, we do not observe absorption (the noise level is marked by the horizontal dashed line). In contrast, when large-amplitude modulation is applied, absorption is partially recovered due to forced spin relaxation at a controlled rate κ_{exp} , as shown by the red peak in the figure. Figure 3(c) was obtained in the plateau center without electron cycling technique, showing on-resonance absorption as a function of incident laser power. At 100 mT (blue squares), relative absorption is 1 order of magnitude weaker than at 0 mT (red circles) due to OSP. In both cases, absorption exhibits weak dependence on laser power. This dependence arises from saturation at high power levels, while the experimental parameters extracted via this method are from the power regime of Fig. 3(a) well below saturation.

D. Peak shift in the plateau center

Figure 4 shows laser scans obtained at $B_z=150$ mT on the blue [Fig. 4(a)] and red [Fig. 4(b)] Zeeman transition throughout the whole single-electron plateau. Absorption strength is color coded. The line tilt is due to the quantum-

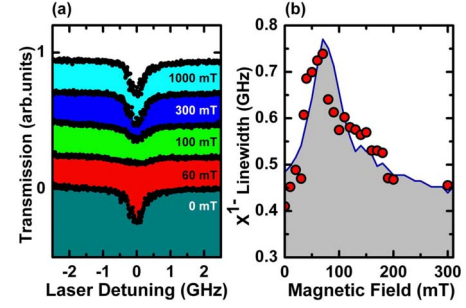


FIG. 5. (Color online) (a) Trion transition laser scans for five different magnetic fields. The gate voltage was in the cotunneling regime (see Appendix A 2). (b) Measured linewidth obtained from laser scans as a function of magnetic field (indicated by the red circles). A broadening occurs at $B_z \approx 75$ mT; at larger fields, the linewidth almost recovers back its original value of 450 MHz at 0 T. The solid line is obtained via numerical simulation with parameters $\Omega_R=0.6\Gamma$, $B_{\text{nuc}}=15$ mT, $\Gamma^{-1}=0.8$ ns, $\gamma_{\text{hm}}^{-1}=2.0$ μs , and $\kappa^{-1}=2.5$ μs .

confined Stark effect and the abscissa pixelization is due to gate-voltage steps during each scan. At gate voltages of 395 and 480 mV, the two cotunneling regimes show strong absorption when spin relaxation is fast due to charge reservoir coupling (for details, refer to Appendix A). In the plateau center, hyperfine interaction dominates and leads to spin pumping and drop of absorption as already discussed. Here, we further observe a shift of the spectral position of the absorption peak in the plateau center as compared to the cotunneling regime. This shift is directed to the red (blue) for the blue (red) Zeeman transition. This resembles effects one might expect for dynamical nuclear spin polarization^{32,33} (DNSP), these effects can, however, be excluded.³⁴ Our numerical simulation is able to reproduce this behavior without taking into account DNSP, as shown in Figs. 4(c) and 4(d). The line shift in the plateau center is ± 0.9 GHz for both red and blue transitions, which is close to the electronic Zeeman splitting at 150 mT, $E_{z,e} \approx 1.3$ GHz. At the cotunneling edges, κ is large and the maximum of absorption is observed when the laser is exactly on-resonance with the transition. When κ is small, as it is the case in the plateau center, absorption of a strictly resonant laser is suppressed due to spin pumping, depending on the external magnetic field. When the laser frequency is moved toward the center between the strong $\tilde{\Gamma}$ and the weak $\tilde{\gamma}$ transitions, i.e., the spectral detuning with respect to the $\tilde{\gamma}$ transition is reduced, the back-pumping at rate $R_{1 \rightarrow 2}$ becomes more efficient, and maximum of absorption will be reached for a spectral detuning that fulfills the condition $R_{1 \rightarrow 2} = R_{2 \rightarrow 1}$. As a consequence, both transitions contribute to absorption, which leads to a shift of the absorption maximum toward the weak $\tilde{\gamma}$ transition, i.e., a blueshift when the red line is observed and vice versa.

E. Peak broadening at plateau edges

Figure 5(a) shows example laser scans for different magnetic fields B_z ranging from 0 to 1 T, obtained in the cotunneling regime where spin relaxation is fast. The scans have

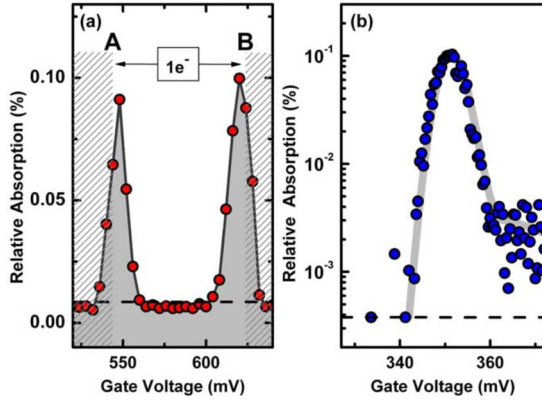


FIG. 6. (Color online) (a) Example voltage coarse scan across the entire single-electron plateau at $B_z=300$ mT. Per voltage step, a laser scan is performed and the observed absorption maximum is plotted as a function of gate voltage. Due to strong hyperfine-induced OSP and weak cotunneling, rate absorption in the plateau center is suppressed; however, when approaching the single-electron plateau edges, absorption is recovered due to highly non-linear dependence of cotunneling on gate voltage, leading to fast spin flips. Outside the voltage plateau, i.e., left of point A or right of point B, absorption is suppressed because the QD then becomes either empty or doubly charged, which shifts the optical transition energies out of our spectral observation window of 30 GHz. The solid line is a guide for the eye. (b) shows a voltage fine scan of the left cotunneling regime obtained on another QD than in (a). The solid line is a numerical calculation using $\Gamma^{-1}=0.8$ ns, $\Omega_R=0.6\Gamma$, $B_{\text{nuc}}=15$ mT, $\Gamma_{\text{tunnel}}^{-1}=20$ ns, $\gamma_{\text{hm}}^{-1}=2$ μ s, and electronic Zeeman splitting $E_{Z,e}=10$ μ eV. The voltage full width at half maximum (FWHM) of the cotunneling peak is 10 mV.

been laterally shifted in order to eliminate the Zeeman shift. In Fig. 5(b), the measured linewidths are plotted as a function of magnetic field (red circles) along with a calculated curve (solid line). A broadening to almost double the zero-field linewidth appears at magnetic fields between 60 and 80 mT; at higher fields, linewidth becomes as narrow as in the case $B_z=0$.

The physical reason for the observed broadening is very similar to that described in Sec. III D: Both $\tilde{\gamma}$ and $\tilde{\Gamma}$ transitions contribute in a non-negligible way to absorption, and a maximum is observed when $R_{1\rightarrow 2}=R_{2\rightarrow 1}$ condition is fulfilled. Consistently, the linewidth increases as much as the electronic Zeeman splitting initially, but drops at magnetic fields where $\tilde{\Gamma}(B)\gg\tilde{\gamma}(B)$ and a single transition is established. In contrast to Sec. III D, κ is large here due to cotunneling and annihilates the absorption drop caused by spin pumping, hence making the transition visible at all magnetic fields. The solid line is a calculated curve using a randomly fluctuating Overhauser field with $B_{\text{nuc}}=15$ mT, well reproducing this feature. We note that in order to put as many constraints as possible on the choice of simulation parameters, we have used the maximum cotunneling-induced spin-relaxation rate $\kappa=\kappa_{\text{cotunnel}}=0.4$ μ s $^{-1}$ as obtained from the data shown in Fig. 6(b). We find that the effect of γ_{hm} , i.e., ϵ_H , on the simulation is negligible, advocating that the dominant OSP mechanism is hyperfine interaction.

F. Coupling to electron spin reservoir

We have performed laser scans as a function of gate voltage throughout the whole single-electron plateau as defined in Appendix A. The measured on-resonance absorption signal for each laser scan is plotted in Fig. 6(a). The data have been obtained at an external magnetic field of $B_z=300$ mT taking coarse voltage steps.

At gate voltages lower than 540 mV and higher than 625 mV, as marked by the shaded regions, absorption drops below noise level indicated by the horizontal dashed line. At these voltages, the QD either becomes empty (left of point A) or doubly charged (right of point B). Absorption then vanishes since, in those cases, the QD is not described by the trion level system anymore; the optical transitions for these gate voltages are not observed within our scanning window of 30 GHz around the trion transitions. The unshaded part indicates the region where the QD contains a single electron and, as it has been mentioned before, the cotunneling rate is maximum when gate voltage is at the crossover points A or B. Here, relaxation via cotunneling is faster than the optical pumping rates $\kappa_{\text{cotunnel}}\gg R_{1\rightarrow 2}, R_{2\rightarrow 1}$, leading to thermalization of the electron spin and, thus, strong absorption. The scenario drastically changes when gate voltage is tuned to the center of the plateau. Here, co-tunneling rate κ_{cotunnel} reaches its minimum, where our numerical calculation predicts a drop of as much as 5 orders of magnitude (also see Fig. 10) compared to the crossover points such that $\kappa_{\text{cotunnel}}\ll R_{2\rightarrow 1}$. Consequently, the occupation of the spin states is governed by OSP [Eq. (8)] rather than Boltzmann factor, meaning that the spin is predominantly in the dark state and vanishing absorption is observed.

The semilogarithmic plot in Fig. 6(b) shows a voltage fine scan of the low voltage plateau edge around the A crossover point obtained at $B_z=300$ mT. The gate voltage for point A is different from Fig. 6(a) as these data were taken on another QD. The observed absorption drops by half within a gate voltage detuning of ± 5 mV from the maximum position. These data demonstrate a giant gate-voltage dependence of this spin-relaxation mechanism. The gray solid line is a best-fit numerical simulation using expression (A6) as spin-relaxation rate, showing good accordance with the data. The cotunneling rate at the peak as determined from the fit is $\kappa_{\text{max}}^{-1}=2.5$ μ s. The noise level is indicated by the dashed line; it deviates from the one shown in Fig. 6(a) due to different experimental settings such as lock-in time constants and filter slopes. Again, on the left side of the peak, the QD is empty, yielding vanishing absorption below the noise level. The gradual decrease of absorption is due to finite temperature. On the right side, the spin pumping regime is located; here, some weak absorption remains according to the occupation of the observed spin state, revealing the strength of spin pumping.

G. Coupling to phonon reservoir

Based on the theoretical estimates of Appendix A, we now seek for signatures of the last remaining reservoir-induced spin dynamics, i.e., spin-orbit (SO)-phonon assisted spin relaxation at high magnetic fields. Figure 7(a) shows

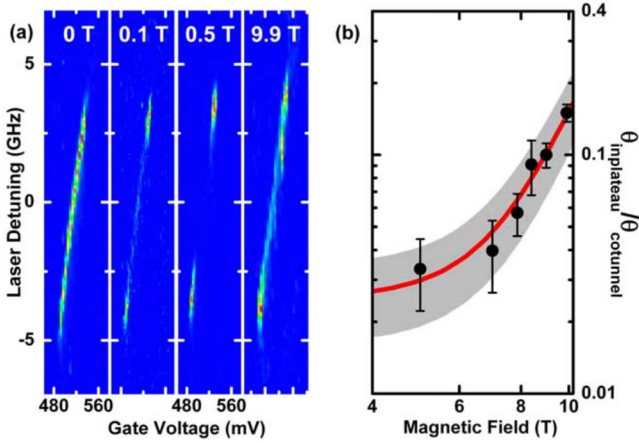


FIG. 7. (Color online) (a) Plateau laser scans for four different magnetic fields: Absorption is plotted as a function of laser detuning and gate voltage. Zeeman effect has been eliminated by vertical shift of each single plot. The linear voltage dependence is due to quantum-confined Stark effect. Plateau-center absorption drops at intermediate magnetic fields due to OSP, but then recovers at high fields due to fast thermalization via phonon-SO interaction at 9.9 T. At the plateau edges, the QD can absorb at all magnetic fields due to fast κ_{cotunnel} . (b) Black data points: Magnetic-field evolution of peak absorption in the plateau center normalized to peak absorption in the cotunneling regime. The lower (upper) boundary of the gray region is obtained from a numerical simulation for $\gamma_{hm}^{-1}=1.2 \mu\text{s}$ ($\gamma_{hm}^{-1}=2.8 \mu\text{s}$); the red line corresponds to $\gamma_{hm}^{-1}=2 \mu\text{s}$. Best match with the data yields explicitly for the spin-relaxation rate $\kappa_{\text{phonon}} = \alpha_0 B_z^5$ with $\alpha_0=0.031$ in units of $\text{T}^{-5} \text{s}^{-1}$. Again, $B_{\text{nuc}}=15 \text{ mT}$.

two-dimensional (2D) plots of color-coded absorption strength as a function of laser detuning and gate voltage for four different magnetic fields obtained for the red Zeeman transition. The scans cover the whole single-electron plateau; excitonic Zeeman shift has been eliminated by shifting the y scale for each 2D graph separately. The linear dependence of the excitonic transition energy on gate voltage is due to the quantum-confined stark shift.

At 0 T, absorption is clearly visible throughout the whole plateau due to fast spin flips with the neighboring nuclear spins. When a small magnetic field ($B=0.1 \text{ T}$) is applied, absorption in the plateau center drops because of hyperfine-induced OSP, as discussed in the previous sections. Close to the plateau edges, absorption still remains due to fast cotunneling. At 0.5 T, increasing OSP leads to further drop of absorption. These absorption characteristics in the plateau center remain the same up to 5 T; however, absorption starts to come back at even higher fields: when the magnetic field is raised up to 9.9 T, a significant recovery of plateau-center absorption is observed. This effect cannot be explained by OSP, which only causes monotonous decrease of absorption, nor by cotunneling, which is negligible in the plateau center and hardly shows any magnetic-field dependence. Owing to its B_z^5 dependence, however, phonon-assisted spin relaxation is a good candidate for the origin of the observed effects in the context of spin-relaxation mechanisms.

Figure 7(b) shows the quantitative evolution of normalized absorption with magnetic field, i.e., the ratio of absorp-

tion in the plateau center versus cotunneling regime (black data points). Further, the solid red line along with the gray shaded region indicates the calculated strength of absorption for $\gamma_{hm}^{-1}=2 \mu\text{s}$ with an uncertainty of $\pm 0.8 \mu\text{s}$; the phonon-induced spin-relaxation rate was $\kappa_{\text{phonon}} = \alpha_0 B_z^5$, with the coefficient $\alpha_0=0.031$ in units of $\text{T}^{-5} \text{s}^{-1}$. Whereas κ_{phonon} is strongly B dependent, the hole-mixing contribution γ_{hm} has no B dependence within the magnetic-field range considered here. Therefore, these two mechanisms have distinguishable effects on Fig. 7(b) and, thus, can be identified independently. The good agreement with the experimental data strongly suggests that in this regime of electric and magnetic fields, the dominant spin relaxation is, indeed, phonon assisted. Further, within our uncertainty, κ_{phonon} matches well with the results that have been previously obtained on an ensemble of self-assembled InAs/GaAs QDs.⁷

There are two fundamentally different mechanisms which employ holes to yield OSP: First, hole mixing of strength ϵ_H leads to an admixture of the light hole states to the trion states as discussed in Sec. II C. Second, hole-spin relaxation leads to an incoherent coupling of the trion states contributing to OSP. In Ref. 35, hole spin-relaxation rate is predicted to be below $10^3/\text{s}$ and monotonically increases with magnetic field, which suggests that it is not the main mechanism responsible for OSP. We, therefore, neglect hole spin flips, further assuming that there is no other efficient hole spin-flip mechanism at low magnetic fields. In the first mechanism, OSP is independent of magnetic field and the strength is equal to the hyperfine-induced OSP rate at $\sim 1 \text{ T}$. At higher magnetic fields, the hyperfine-induced OSP rate drops with B_z^{-2} ; therefore, hole mixing becomes the dominant OSP mechanism here.

IV. FULL INTERACTION MAP

In the previous sections, three spin-relaxation mechanisms acting on the confined spin have been identified separately along with the two mechanisms for OSP, both through experimental and theoretical studies. In this final part, we extrapolate our findings numerically to the whole of the relevant external magnetic and electric field phase space in order to predict the longest available single-electron spin-relaxation times within this whole range. The calculations have been performed within a parameter space approximately overlapping with the full scale of our experimental tuning ability of the static electric and magnetic fields. For details of the simulation, we refer to Appendix E.

Figure 8 shows calculated maximum values of absorption for the red [Fig. 8(a)] and the blue [Fig. 8(b)] trion transition with a laser having the corresponding circular polarization. Absorption strength is color coded in logarithmic scale as a function of gate-voltage detuning and external magnetic field.

All of the following points have been discussed in the previous sections; here, we mention them briefly as a key to the plots: the necessary conditions for observing strong absorption are either $\kappa \gg R_{1 \rightarrow 2}, R_{2 \rightarrow 1}$ or $R_{1 \rightarrow 2} \sim R_{2 \rightarrow 1}$. Further, at large magnetic fields $B_z > 8 \text{ T}$ when electronic Zeeman splitting $E_{Z,e} \sim kT$, the Boltzmann factor leads to a difference

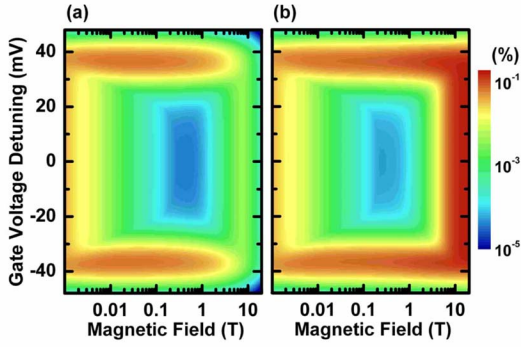


FIG. 8. (Color online) Calculated absorption maxima for the whole single-electron plateau plotted as a function of magnetic and electric fields. (a) shows the simulation for the probe laser in the vicinity of the red Zeeman transition; (b) similar but for the blue Zeeman transition. The borders of each plot show strong absorption due to interactions with nuclear spins (left), charge reservoir (top/bottom), and phonon reservoir (right). At large magnetic fields, spin polarization nearly reaches unity due to thermalization, leading to vanishing absorption on the red transition (a) and enhanced absorption on the blue transition (b). In the center of the plots, absorption, and thus spin relaxation, is suppressed by approximately 5 orders of magnitude. The parameters used in the simulation are $\Gamma^{-1}=0.8$ ns, $B_{\text{nuc}}=15$ mT, $\gamma_{\text{hm}}^{-1}=2$ μ s, tunneling time $\Gamma_{\text{tunnel}}^{-1}=20$ ns, and κ_{phonon} as given in Sec. III G.

of the spin ground-state occupations and, thus, a difference between absorption strengths on the red and blue Zeeman transitions.

In the plot, we distinguish three different regimes of strong absorption:

(1) *Magnetic fields lower than the fluctuations of the hyperfine field* ($B_z \lesssim 15$ mT). Here, fast bidirectional OSP due to hyperfine-induced state mixing leads to strong absorption.

(2) *High magnetic fields* (>5 T). Here, κ_{phonon} induces fast thermalization, i.e., $\kappa_{\text{phonon}} \gg R_{1 \rightarrow 2}, R_{2 \rightarrow 1}$. The spin ground-state occupation is mainly determined by the Boltzmann factor, leading to a lowering (increase) of absorption on the higher (lower) energy spin state occupation (a) [(b)].

(3) *Large gate-voltage detunings from the plateau center* (± 40 mV). Here, cotunneling (κ_{cotunnel}) is responsible for fast spin relaxation and appearance of absorption.

An intriguing feature that becomes apparent now is the blue *island* in the center of the color-coded spin-relaxation plot. It marks the regime where absorption (i.e., all reservoir interactions) is suppressed by 5 orders of magnitude or, in other words, the localized spin becomes maximally isolated, hence the frequently used concept of an *artificial atom* is meaningful. Within the scope of quantum information processing, this indicates the relevant regime of operation where a spin-relaxation time of up to 1 s is predicted.

V. SUMMARY AND CONCLUSION

We have investigated the dominant interactions of a confined electron spin in a single self-assembled QD by optical means and demonstrated the regimes where each reservoir

coupling becomes important. For magnetic fields $B_z \lesssim 1$ T, the dominant contribution to OSP stems from the fluctuating hyperfine field mixing the electronic spin states and creating a weak channel for diagonal relaxation in the trion four-level picture. Exchange and phonon-induced spin-flip processes dominate over hyperfine-induced spin pumping and establish a thermal steady state at large gate-voltage detunings and/or large external magnetic fields; in the plateau center at intermediate magnetic fields, the situation is reversed and spin pumping dominates, strongly altering the state occupations away from thermal equilibrium values. Signatures of heavy-light hole mixing dominated spin cooling can be observed for fields $\gtrsim 5$ T.

From a quantum control perspective, these results demonstrate that the quantum dynamics of a single confined spin can be significantly altered by externally controlled parameters such as electric and magnetic fields. A natural extension of this study would be the investigation of spin decoherence in a single QD using similar optical techniques. These measurements would require more advanced schemes such as electromagnetically induced transparency. Further, knowledge gained on single-electron spin dynamics can be utilized in the resonant optical study of more complex systems such as coupled QDs or QDs with a single excess heavy hole.

ACKNOWLEDGMENTS

We thank Hakan Türeci, Alex Högele, Tunc Yilmaz, Je-roen Elzerman, and Nick Vamivakas for useful discussions. This work is supported by NCCR Quantum Photonics. J.D. and M.A. would like to thank J. Cash for technical assistance.

APPENDIX A: RESERVOIR COUPLINGS OF THE QUANTUM DOT SPIN

1. Nuclear spins

The interaction of a localized electron spin with a surrounding nuclear spin ensemble can be written in the form of the Fermi contact interaction^{12,13,29,36} $\hat{H}_{\text{hyp}} = \frac{\nu_0}{8} \sum_i A_i |\psi(\mathbf{R}_i)|^2 (\hat{\mathbf{I}}_i \cdot \hat{\boldsymbol{\sigma}})$. The sum runs over all nuclei i in the lattice. ν_0 is the volume of an InAs unit cell, $\psi(\mathbf{R}_i)$ the electron envelope wave function at the i th nucleus, and $\hat{\mathbf{I}}_i$ and $\hat{\boldsymbol{\sigma}}$ are the spin operators of nuclear and electron spins. A_i is the hyperfine coupling strength determined by the value of the electron Bloch wave function at the site of each nucleus. The total number of nuclei in our InAs/GaAs QDs can be estimated to be $N=10^4-10^5$.

We can equivalently describe the effect of hyperfine interactions with an effective magnetic field seen by the QD spin, which is commonly referred to as *Overhauser field* $\mathbf{B}_N = \frac{\nu_0}{8} \frac{\bar{A}}{g_e \mu_B} \langle \sum_i \hat{\mathbf{I}}_i \rangle$, where \bar{A} is an average spin-nuclei coupling constant. Due to the arbitrary direction of the Overhauser field, the spin ground states become admixed. The excited (excitonic) states remain unaffected due to the p -like symmetry of the hole Bloch wave function and to the two elec-

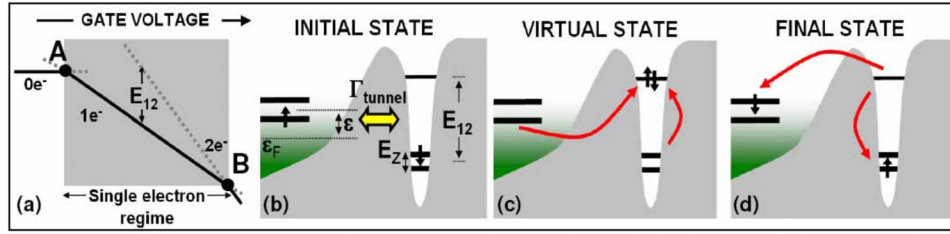


FIG. 9. (Color online) (a) *Stability diagram* of the QD ground states neglecting spin: Energies of the zero-, one-, and two-electron QD as a function of gate voltage. Crossover points are marked A and B. E_{12} denotes the gate-voltage-dependent energy difference between the singly charged and doubly charged states or charging energy. [(b)–(d)] The QD can exchange its single electron with the charge reservoir via a virtual empty or two-electron (shown here) state. When one of the two singlet electrons tunnels out, it leaves the remaining QD spin in a mixed state equivalent to spin relaxation. Γ_{tunnel} marks the tunneling rate through the 35 nm GaAs barrier, and ε the detuning from the Fermi energy ε_F . E_z is the electronic Zeeman splitting, and E_{12} the energy required to charge a second electron.

trons forming a singlet which is immune to magnetic-field variations.

In order to further understand the effect of the hyperfine field in optical experiments, we consider two regimes: First, an external magnetic field with strength smaller than the hyperfine field is applied or the external field is completely absent. Hence, the direction of the total magnetic field seen by the electron spin is fully random after a nuclear field correlation time. As we saw in Sec. II, fast bidirectional OSP is the consequence of inducing efficient spin relaxation to dominate over other mechanisms.²⁹ In the second regime, the applied external field is much stronger than the hyperfine field. In this case, the electron spin mainly sees the external magnetic field along the z axis and the hyperfine field only leads to small fluctuations of the nuclear field vector. In this regime, the light-induced spin relaxation is slow and other mechanisms can be dominant.

For the experiments described in this paper, we can treat the hyperfine field as a purely classical field $\mathbf{B}_N(t)$ with correlation time $\tau_{\text{corr}} \sim 1$ ms. The correlation time is expected to be similar to the decay time of nuclear spin polarization in the presence of a QD electron and in the absence of external magnetic field, as measured in Ref. 37. B_{nuc} refers to the rms value of the Gaussian distribution as defined by

$$f(\mathbf{B}_N) = \frac{1}{B_{\text{nuc}}^3 (2\pi)^{3/2}} \exp\left(-\frac{|\mathbf{B}_N|^2}{2B_{\text{nuc}}^2}\right), \quad (\text{A1})$$

which yields $\langle \mathbf{B}_N(t) \rangle = 0$ and $\langle |\mathbf{B}_N(t)|^2 \rangle = 3B_{\text{nuc}}^2$. Here, $\langle \rangle$ denotes the time average over many correlation times. B_{nuc} can be written in the form

$$B_{\text{nuc}} = \frac{b_0}{\sqrt{N}}, \quad (\text{A2})$$

with b_0 a parameter characterized by the species of nuclei and the composition of the QD,³⁸ and N the number of nuclear spins interacting with the QD spin.

The QD composition is taken to be 90% InAs and 10% GaAs, yielding $I(I+1) = 13.2$ when averaging over the different nuclear species.³⁹ Similarly, we obtain $A^2 = 2500 \mu\text{eV}^2$, which yields $b_0 = 3.0$ T. Using Eq. (A2) with $N = 10^4 - 10^5$ nuclear spins, we obtain for our QDs $B_{\text{nuc}} = 9.5 - 30$ mT. As our $\mathbf{B}_N(t)$ is classical, we treat the $B_{N,i}(t)$ with $i = x, y,$ and z

as independent random variables. Here, the component of the nuclear field along the z axis $B_{N,z}(t)$ only leads to Zeeman splitting, whereas the in-plane components induce a mixing of the $|\uparrow\rangle$ and $|\downarrow\rangle$ states. The in-plane hyperfine field is

$$B_{N,xy}^2(t) = B_{N,x}^2(t) + B_{N,y}^2(t), \quad (\text{A3})$$

and we define

$$\hbar\Omega_H(t) = \frac{g_e \mu_B B_{N,xy}(t)}{2}. \quad (\text{A4})$$

We note here that our measurement time (typically 10–100 ms) is longer than the correlation time of the nuclear field; i.e., for each measured data point, we expect that we average over many configurations of the nuclear magnetic field.⁴⁰

2. Coupling to electron spin reservoir

The exchange interaction with the Fermi sea in the back contact (sample details are in Appendix B) can be written as

$$\hat{H}_{\text{charge}} = \sum_{k,k'} \hbar g_{t,k} (e_{k,\downarrow}^\dagger e_{QD,\uparrow}^\dagger e_{QD,\downarrow} e_{k',\uparrow} + \text{c.c.}), \quad (\text{A5})$$

where $e_{QD,\sigma}^\dagger$ and $e_{QD,\sigma}$ are the creation and annihilation operators for an electron with spin σ in the QD, and similarly in the reservoir. $g_{t,k}$ is the tunneling matrix element, which is linked to the tunneling rate Γ_{tunnel} by Fermi's golden rule $\Gamma_{\text{tunnel}} = \frac{2\pi}{\hbar} |g_{t,k}|^2 \rho(E)$, with $\rho(E)$ being the density of states in the back contact. It is well known that exchange interaction of a confined spin with an electron spin reservoir gives rise to spin-flip cotunneling^{41,42} at our operating temperatures ($T \sim 4$ K); at temperatures lower than the Kondo temperature T_K , it leads to the formation of a Kondo singlet.^{43–46}

Figure 9(a) shows the energies of the empty, singly, and doubly charged QD state as a function of gate voltage.⁴⁷ Which state has the lowest energy obviously depends on the gate voltage, and the QD attempts to reach it by either attracting or repelling electrons from or into the reservoir. Clearly, there is a range of voltages (*single-electron charging plateau*) where it is energetically favorable for the QD to accommodate a single electron, marked by the shaded region

in the figure. At the points A and B, two charging levels are degenerate and fast exchange of the QD electron with the reservoir can take place, only limited by the tunneling rate. The *real* gate voltages V_A and V_B that need to be applied in order to reach points A and B can vary from dot to dot, depending on its confinement properties. We define the plateau center $V_c = \frac{V_B - V_A}{2}$. The gate-voltage detuning is $\Delta V_g = V_g - V_c$. The schematic cotunneling process is depicted in Figs. 9(b)–9(d). The initial state is characterized by a QD with a single spin-down electron, and Coulomb blockade prohibits tunneling of further electrons into the dot [Fig. 9(b)]. Together with a spin-up electron from the reservoir, a virtual spin singlet [Fig. 9(c)] is formed at energy difference $\Delta E = \varepsilon + E_{12}$, where ε is the detuning from the reservoirs' Fermi energy ε_F . Finally, the QD returns to the singly charged state with a spin-up electron [Fig. 9(d)].

E_{12} is given by $E_{12} = E_2 - E_1 = e \frac{(V_B - V_g)}{\lambda}$ and $E_{01} = E_1 - E_0 = e \frac{(V_g - V_A)}{\lambda}$, with E_i the energy of the QD charged with i electrons and λ a constant describing the geometric lever arm of the heterostructure.

Using Eq. (A5), one obtains for the cotunneling rate in second order^{42,48}

$$\kappa_{\text{cotunnel}} = \hbar \Gamma_{\text{tunnel}}^2 \int_{\varepsilon} \left| \frac{1}{\frac{e(V_g - V_A)}{\lambda} + \varepsilon + \frac{i}{2} \hbar \Gamma_{\text{tunnel}}} + \frac{1}{\frac{e(V_B - V_g)}{\lambda} - \varepsilon + \frac{i}{2} \hbar \Gamma_{\text{tunnel}}} \right|^2 f(\varepsilon) [1 - f(\varepsilon)] d\varepsilon. \quad (\text{A6})$$

The integral is the sum over all second-order transitions with different detunings ε from the Fermi energy according to Figs. 9(b)–9(d). In addition, the term with $e(V_g - V_A)/\lambda = E_{01}$ describes the related process where the virtual state is an empty QD. $f(\varepsilon)$ is the Fermi function $f(\varepsilon) = 1/[1 + \exp(\varepsilon/kT)]$. Expression (A6) is valid under the condition $E_{Z,e} \ll kT$, i.e., for low magnetic fields. To obtain the exact expression for all magnetic fields, the Fermi function terms in the integral have to be modified.⁴⁹

The imaginary part of the denominator introduces a finite lifetime to the electronic states limited by the tunneling rate Γ_{tunnel} , implying that the main cause for broadening of the spin ground states is tunneling. This is relevant for elements of the integral with vanishing real part.

In order to obtain an estimate for the cotunneling times in our structure, we use results obtained on samples with 25 nm tunneling barrier where in certain gate-voltage regimes tunneling rate is larger than radiative recombination rate, i.e., $\Gamma_{\text{tunnel}} > \Gamma$, leading to broadening in the linewidths observed in photoluminescence measurements.⁴⁸ Then from a Wentzel-Kramers-Brillouin estimation of the two different tunneling barriers together with the measured tunneling rate, we estimate the tunneling rate Γ_{tunnel} to be on the order of 0.02–0.1 ns⁻¹ in our structure. We take it to be independent of the gate voltage within the single-electron regime. Figure 10 shows the calculated cotunneling rate obtained with ex-

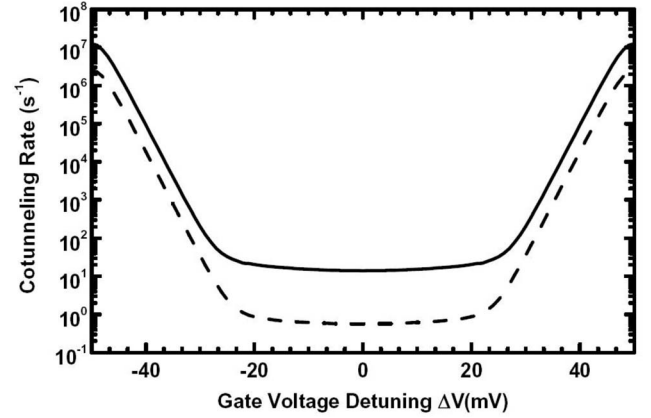


FIG. 10. Expected cotunneling rate obtained using expression (A6) with the parameters $\Gamma_{\text{tunnel}} = 0.1 \text{ ns}^{-1}$ (solid curve) and $\Gamma_{\text{tunnel}} = 0.02 \text{ ns}^{-1}$ (dashed curve), $V_A = -50 \text{ mV}$, $V_B = +50 \text{ mV}$, $kT = 300 \mu\text{eV}$, and $\lambda = 5.3$.

pression (A6) using two different tunneling rates of $\Gamma_{\text{tunnel}} = 0.02 \text{ ns}^{-1}$ and $\Gamma_{\text{tunnel}} = 0.1 \text{ ns}^{-1}$ representing the minimum and the maximum cotunneling rate we expect in our experiments respectively. Cotunneling rate is characterized by its very nonlinear voltage dependence. When close to the crossover points V_A and V_B , it exhibits an ultrasteep slope; in contrast, the voltage dependence is weak in the plateau center V_c .

3. Spin-phonon interaction

It is known that spin relaxation in higher-dimensional systems is mainly due to SO interaction in conjunction with phonons.^{50,51} Despite being strongly suppressed, SO interaction is still an enabling mechanism for phonon-assisted spin flips in QDs and a considerable amount of theoretical work has been done on this spin-relaxation mechanism.^{28,51–54} SO coupling is a well-known phenomenon in atomic physics as well as in semiconductors and is, in general, characterized by an interaction term of type $H_{SO} = \sum_{i,j} a_{ij} \hat{l}_i \hat{\sigma}_j$, with \hat{l} the angular momentum operator and $\hat{\sigma}$ the spin operator of the electron; the sum runs over all pairs $i, j = x, y, \text{ and } z$.

The resulting spin-relaxation rate is a function of magnetic field and is given by

$$\kappa_{\text{phonon}} = \frac{(g_e \mu_B B_z)^5}{\hbar (\hbar \omega_0)^4} \Lambda_p, \quad (\text{A7})$$

where $\hbar \omega_0$ is the quantization energy for electrons and Λ_p a dimensionless constant describing the strength of the piezoelectric coupling. The B_z^5 dependence valid for electronic Zeeman splitting $E_{Z,e} \gg kT$ becomes replaced by $B_z^4 kT$ when $E_{Z,e} \ll kT$, due to the Boltzmann factor in Eq. (C1).^{51,52}

In addition to this dominant mechanism, there are numerous other ways of *direct* spin-phonon coupling which turn out to be orders of magnitude weaker than the admixture mechanism described above⁵¹ and are not considered in our treatment. Likewise, two-phonon processes with characteristically strong temperature dependence^{28,53} ($T^7 - T^{11}$) are also

rather weak and not included here. Finally, it has been proposed that phonons together with the hyperfine-induced mixing of the Zeeman s levels lead to relaxation of the QD spin. As already mentioned in Sec. II, this mechanism is also inefficient and the resulting rate is predicted to depend on the external magnetic field as $\sim B_z^3$ (Ref. 29): according to the calculations presented in Ref. 27, the rate will be less than $\kappa \sim 1 \text{ s}^{-1}$ at a magnetic field of 1 T when considering the larger quantization energy in our QDs. Based on these arguments, we proceed with considering only the mechanism leading to Eq. (A7).

APPENDIX B: SAMPLE AND EXPERIMENTAL TECHNIQUES

Our InAs/GaAs QDs are grown by molecular beam epitaxy in Stranski-Krastanow mode, leading to lens-shaped dots of average size $25 \times 25 \times 5 \text{ nm}^3$; QD light emission is blueshifted by partially covered islands technique. A 35 nm GaAs tunneling barrier separates the QDs from a charge reservoir formed by a heavily doped n -GaAs layer which forms the back contact. Above the QDs, there is a 12-nm-thick GaAs cap and a 50-nm-thick $\text{Al}_{0.4}\text{Ga}_{0.6}\text{As}$ blocking layer which prevents the holes from coupling to the continuum states within the 88 nm capping layer.⁴⁷ Bias voltage between the back contact and a semitransparent 5 nm Ti-Schottky window determines the electric field in the structure and allows us to load a single conduction-band electron into the QD.

All experiments described here are carried out with a confocal microscopy setup immersed in a liquid helium bath cryostat at a temperature of 4.2 K. The numerical aperture of the microscope is 0.68, resulting in a diffraction limited spot size of $\sim 1 \mu\text{m}$. Area density of QDs in our sample is low enough to have ≤ 3 dots in the focal spot simultaneously. Transmitted light is collected and sent to a circular polarization analyzer which distributes the light to two photodetectors, similar to that of Ref. 11.

The initial step of our experiment is a gate sweep, i.e., a PL measurement as a function of gate voltage as shown in Fig. 11(a). For this we send in a laser, exciting electrons and holes in the bulk GaAs at an energy of $\approx 1.6 \text{ eV}$. QD luminescence is sent to a grating spectrometer with a resolution $\sim 20 \mu\text{eV}$.

Hereafter, the differently charged excitonic complexes can be identified by their characteristic emission energy and voltage dependence profile.⁵⁵ From then on, we only apply resonant excitation of the QD single-electron ground-state transitions by using a DT technique.^{23–26} In order to obtain a spectrum, we sweep a single-mode Ti:sapphire laser over the QD transition and record the intensity of the transmitted light. A QD resonance is observed as a dip on top of the laser background [see Fig. 11(b)]. The resolution of this technique is only limited by the laser linewidth, i.e., $\Delta\nu_{\text{laser}} < 1 \text{ MHz}$.

APPENDIX C: OPTICAL BLOCH EQUATIONS FOR THE THREE-LEVEL SYSTEM

The master equation for the system (reduced) density operator $\hat{\rho}$ reads $\frac{d}{dt}\hat{\rho} = \frac{1}{i\hbar}[\hat{H}_0, \hat{\rho}] + \hat{L}_{\text{relaxation}}$, where the term \hat{H}_0

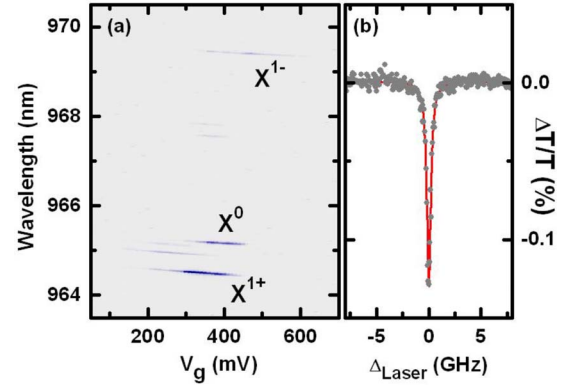


FIG. 11. (Color online) (a) Example gate sweep. This plot has been obtained by increasing the gate voltage step by step and for each step taking a single-QD photoluminescence (PL) spectrum. The three strongest emission lines are identified as X^0 , X^{1-} , and tentatively X^{1+} , which result from s -shell electron-hole recombination from differently charged excitonic complexes. Small continuous PL energy shift is due to quantum-confined stark shift. (b) Example differential transmission laser scan. On resonance, Rayleigh-scattered light interferes with the laser background and results in a dip in the intensity measurement. The FWHM of the Lorentzian fit indicated by the solid red line is 460 MHz.

$= \hat{H}_{\text{Zeeman}} + \hat{H}_{\text{int,rad}}$ describes the unitary dynamics and $\hat{L}_{\text{relaxation}}$ results from the interactions with reservoirs.

After adding the relaxation terms due to the coupling to the thermal bath of radiation field modes (spontaneous emission terms) at rate Γ , the relaxation terms in the Lindblad form are⁵⁶

$$\begin{aligned} \hat{L}_{\text{relaxation}} = & \frac{\Gamma}{2}(2\hat{\sigma}_{23}\hat{\rho}\hat{\sigma}_{32} - \hat{\sigma}_{33}\hat{\rho} - \hat{\rho}\hat{\sigma}_{33}) + \frac{\kappa}{2}\bar{n}(2\hat{\sigma}_{12}\hat{\rho}\hat{\sigma}_{21} - \hat{\sigma}_{22}\hat{\rho} \\ & - \hat{\rho}\hat{\sigma}_{22}) + \frac{\kappa}{2}(\bar{n} + 1)(2\hat{\sigma}_{21}\hat{\rho}\hat{\sigma}_{12} - \hat{\sigma}_{11}\hat{\rho} - \hat{\rho}\hat{\sigma}_{11}). \end{aligned} \quad (\text{C1})$$

Here, $\hat{\sigma}_{ab} = |a\rangle\langle b|$ is the projection operator. At temperatures smaller or comparable to the electronic Zeeman splitting $kT < E_{Z,e}$, a Boltzmann factor $\bar{n} = 1/[\exp(g_e\mu_B B/kT) - 1]$ needs to be taken into account, which leads to thermalization of the electron spin, i.e., in the absence of light, $\rho_{11}/\rho_{22} = \exp(-E_{Z,e}/kT)$, where $E_{Z,e}$ is the electronic Zeeman energy. In the case of exchange coupling, the \bar{n} terms cannot be regarded as an *occupancy*; it can, however, be shown that a similar factor appears in the cotunneling rate (A6) when Zeeman splitting is taken into account.⁵⁷

The optical Bloch equations are derived from the master equation given at the beginning of this paragraph. Including rotating-wave approximation and taking the limit of Zeeman splitting $E_z \ll kT$ which eliminates the Boltzmann factors, the optical Bloch equations read

$$\frac{d}{dt}\rho_{11} = i\Omega_H(\rho_{12} - \rho_{21}) + \gamma_{lm}\rho_{33} - \kappa(\rho_{11} - \rho_{22}),$$

$$\frac{d}{dt}\rho_{22} = i\frac{\Omega_R}{2}(\rho'_{23} - \rho'_{32}) + i\Omega_H(\rho_{21} - \rho_{12}) + \Gamma\rho_{33} + \kappa(\rho_{11} - \rho_{22}),$$

$$\frac{d}{dt}\rho_{33} = i\frac{\Omega_R}{2}(\rho'_{32} - \rho'_{23}) - (\Gamma + \gamma_{hm})\rho_{33},$$

$$\frac{d}{dt}\rho_{12} = i\frac{\Omega_R}{2}\rho'_{13} + i\Omega_H(\rho_{11} - \rho_{22}) - \kappa\rho_{12},$$

$$\frac{d}{dt}\rho'_{13} = i\frac{\Omega_R}{2}\rho_{12} - i\Omega_H\rho'_{23} + \left(-\frac{\Gamma + \gamma_{hm} + \kappa}{2} - i\delta\omega\right)\rho'_{13},$$

$$\frac{d}{dt}\rho'_{23} = i\frac{\Omega_R}{2}(\rho_{22} - \rho_{33}) - i\Omega_H\rho'_{13} + \left(-\frac{\Gamma + \gamma_{hm} + \kappa}{2} - i\delta\omega\right)\rho'_{23},$$

with

$$\rho_{13} = \rho'_{13}e^{i\omega_L t}, \quad \rho_{23} = \rho'_{23}e^{i\omega_L t}.$$

We have $\rho'_{31} = \rho'_{13}$, $\rho'_{21} = \rho'_{12}$, $\rho'_{32} = \rho'_{23}$, and $\rho_{11} + \rho_{22} + \rho_{33} = 1$.

APPENDIX D: DRESSED-STATE TRANSFORMATION

The transformation used to diagonalize the coupling to the quasistatic nuclear (Overhauser) field can be written as $\tilde{H} = S\hat{H}S^\dagger$ and $\tilde{\rho} = S\rho S^\dagger$, with $\phi = \Omega_H/\omega_z$ and $S^\dagger S = \mathbb{I}$. We assume $\phi \ll 1$. When taking only first-order terms

$$S = \begin{pmatrix} 1 & -\phi & 0 \\ \phi & 1 & 0 \\ 0 & 0 & 1 \end{pmatrix}. \quad (\text{D1})$$

The spontaneous emission terms then yield $SL_{\text{relaxation},\Gamma}S^\dagger = \frac{\Gamma}{2}(2S\sigma_{23}S^\dagger\tilde{\rho}S\sigma_{32}S^\dagger - S\sigma_{33}S^\dagger\tilde{\rho} - \tilde{\rho}S\sigma_{33}S^\dagger)$. For the new projection operator $S\sigma_{23}S^\dagger$, we obtain $S\sigma_{23}S^\dagger = \phi\sigma_{13} + \sigma_{23}$ and the conjugate relation. Here, $\sigma_{ij} = |\tilde{i}\rangle\langle\tilde{j}|$. Using this with the previous relation, we obtain $SL_{\text{relaxation},\Gamma}S^\dagger = \frac{\tilde{\gamma}}{2}(2\sigma_{13}\tilde{\rho}\sigma_{31} - \sigma_{33}\tilde{\rho} - \tilde{\rho}\sigma_{33}) + \frac{\tilde{\Gamma}}{2}(2\sigma_{23}\tilde{\rho}\sigma_{32} - \sigma_{33}\tilde{\rho} - \tilde{\rho}\sigma_{33}) - 2\phi\frac{\Gamma}{2}(\sigma_{23}\tilde{\rho}\sigma_{31} + \sigma_{13}\tilde{\rho}\sigma_{32})$, where $\tilde{\gamma} = \phi^2\Gamma$ and $\tilde{\Gamma} = \Gamma$. $\tilde{\sigma}_{ij} = |\tilde{i}\rangle\langle\tilde{j}|$ is the projection operator acting on $\tilde{\rho}$. The first, $\tilde{\gamma}$ term, corresponds to relaxation via a weak optical transition induced by the hyperfine field, allowing for spin-flip Raman events, and the second, $\tilde{\Gamma}$ term, describes relaxation via the strong optical trion transition.

The last term describes coherence induced by the spontaneous relaxation into a superposition of dressed-basis ground states at a rate proportional to the occupation of the excited state $\tilde{\rho}_{33}$. When multiplying with $\langle 2|$ from the left and $|1\rangle$ from the right, we obtain $\frac{d}{dt}\tilde{\rho}_{21} = -2\phi\Gamma\tilde{\rho}_{33}$. The same relation is obtained for $\tilde{\rho}_{21}$ when multiplying with $\langle 1|$ and $|2\rangle$, respectively.

The transformed κ terms keep the Lindblad form, and we obtain for $E_{z,e} \ll kT$

$$\tilde{L}_{\text{relaxation},\kappa} = \frac{\tilde{\kappa}}{2}[(2\tilde{N}_{21}\tilde{\rho}\tilde{N}_{12} - \tilde{M}_{11}\tilde{\rho} - \tilde{\rho}\tilde{M}_{11}) + (2\tilde{N}_{12}\tilde{\rho}\tilde{N}_{21} - \tilde{M}_{22}\tilde{\rho} - \tilde{\rho}\tilde{M}_{22})], \quad (\text{D2})$$

with $\tilde{N}_{21} = S\sigma_{21}S^\dagger$, $\tilde{N}_{12} = \tilde{N}_{21}^\dagger$, $\tilde{M}_{ii} = S\sigma_{ii}S^\dagger$, and $\tilde{\kappa} = \kappa$.

APPENDIX E: NUMERICAL STUDIES

The derived formalism considers a static randomly oriented nuclear field. Within a measurement time, B_N changes ~ 100 times. In order to calculate measurable quantities such as linewidths and peak heights as functions of electric and magnetic fields, we have, thus, performed numerical simulations: For a given set of parameters, the steady-state solutions of the optical Bloch equations as given in Appendix C are numerically evaluated, in particular $\text{Im}(\rho_{23}(\infty))$ is then linked to the absorption (details in Sec. III). A fluctuating hyperfine field is implemented by pulling three random numbers $B_{N,i}$ following Eq. (A1). From $B_{N,xy}$, using Eq. (A3), state-mixing strength Ω_H (A4) and pure Zeeman splitting ω_z are calculated before evaluating the density matrix steady state. This procedure is repeated in order to average over ~ 100 random settings of the hyperfine field. In the cases, the simulation could not be performed throughout the whole parameter space; we confirmed in key regimes that results agree well with that of a static Overhauser field with equal magnitude in x , y , and z : From Eq. (A4), we obtain for the rms value of $\Omega_H(t)$

$$\langle \Omega_H^2(t) \rangle = \left(\frac{g_e\mu_B}{\hbar}\right)^2 \frac{\langle B_{xy}^2(t) \rangle}{4} = \left(\frac{g_e\mu_B}{\hbar}\right)^2 \frac{B_{\text{nuc}}^2}{2}. \quad (\text{E1})$$

Here, the assumption for the observed absorption Θ to be made is $\langle \Theta(B_{N,xy}^2(t)) \rangle \approx \Theta(\langle B_{N,xy}^2(t) \rangle)$, i.e., the averaging over the absorption strength for different settings of the hyperfine field approximately equals the strength of absorption for the average field magnitude, equal in x , y , and z .

¹J. Elzerman, R. Hanson, L. Van Beveren, B. Witkamp, L. Vandersypen, and A. Kouwenhoven, Nature (London) **430**, 431 (2004).

²S. Amasha, K. MacLean, I. Radu, D. M. Zumbühl, M. A. Kastner, M. P. Hanson, and A. C. Gossard, Phys. Rev. Lett. **100**, 046803 (2008).

³F. Koppens, C. Buizert, K. Tielrooij, I. Vink, K. Nowack, T. Meunier, L. Kouwenhoven, and A. Vandersypen, Nature (London)

442, 766 (2006).

⁴F. H. L. Koppens, J. A. Folk, J. M. Elzerman, R. Hanson, L. H. W. van Beveren, I. T. Vink, H. P. Tranitz, W. Wegscheider, L. P. Kouwenhoven, and L. M. K. Vandersypen, Science **309**, 1346 (2005).

⁵A. Johnson, J. Petta, J. Taylor, A. Yacoby, M. Lukin, C. Marcus, M. Hanson, and A. Gossard, Nature (London) **435**, 925 (2005).

- ⁶J. R. Petta, A. C. Johnson, J. M. Taylor, E. A. Laird, A. Yacoby, M. D. Lukin, C. M. Marcus, M. P. Hanson, and A. C. Gossard, *Science* **309**, 2180 (2005).
- ⁷M. Kroutvar, Y. Ducommun, D. Heiss, M. Bichler, D. Schuh, G. Abstreiter, and J. Finley, *Nature (London)* **432**, 81 (2004).
- ⁸D. Loss and D. P. DiVincenzo, *Phys. Rev. A* **57**, 120 (1998).
- ⁹A. Imamoglu, D. D. Awschalom, G. Burkard, D. P. DiVincenzo, D. Loss, M. Sherwin, and A. Small, *Phys. Rev. Lett.* **83**, 4204 (1999).
- ¹⁰T. Calarco, A. Datta, P. Fedichev, E. Pazy, and P. Zoller, *Phys. Rev. A* **68**, 012310 (2003).
- ¹¹M. Atatüre, J. Dreiser, A. Badolato, A. Högele, K. Karrai, and A. Imamoglu, *Science* **312**, 551 (2006).
- ¹²I. A. Merkulov, A. L. Efros, and M. Rosen, *Phys. Rev. B* **65**, 205309 (2002).
- ¹³J. M. Taylor, J. R. Petta, A. C. Johnson, A. Yacoby, C. M. Marcus, and M. D. Lukin, *Phys. Rev. B* **76**, 035315 (2007).
- ¹⁴From the measured light polarization in our experiment, we obtain that the unwanted σ^- component is suppressed by a factor of 25. An additional factor comes from the optical detuning with respect to the diagonal transition in magnetic field, with the laser being on the strong transition. At $B_z=60$ mT, the detuning leads to a further suppression $\sim 1/50$, altogether suppressing the unwanted excitation of the weak transition by more than 1200 times, increasing with magnetic field. At fields less or on the order of the hyperfine field, spin ground states are strongly mixed, leading to all possible (vertical as well as diagonal) couplings in the four-level scheme, thus creating two differently polarized Λ systems with equal decay rates to both ground states. The presence of the (unwanted and mainly suppressed) σ^- polarized light would just increase the bidirectional OSP by a small amount.
- ¹⁵J. Brossel, A. Kastler, and J. Winter, *Science* **13**, 668 (1952).
- ¹⁶A. Shabae, A. L. Efros, D. Gammon, and I. A. Merkulov, *Phys. Rev. B* **68**, 201305(R) (2003).
- ¹⁷R. Loudon, *The Quantum Theory of Light*, 3rd ed. (Oxford Science, New York, 2003).
- ¹⁸J. M. Luttinger, *Phys. Rev.* **102**, 1030 (1956).
- ¹⁹G. Bester, S. Nair, and A. Zunger, *Phys. Rev. B* **67**, 161306(R) (2003).
- ²⁰This can be seen from $\langle \downarrow \uparrow \uparrow | H_{\text{int,rad}} | \downarrow \downarrow \rangle \neq 0$ as opposed to $\langle \downarrow \uparrow \uparrow | H_{\text{int,rad}} | \downarrow \downarrow \rangle = 0$.
- ²¹K. Karrai and R. J. Warburton, *Superlattices Microstruct.* **33**, 311 (2003).
- ²²A. Högele, Ph.D. thesis, LMU Munich, 2005.
- ²³B. Alen, A. Högele, M. Kroner, S. Seidl, K. Karrai, R. J. Warburton, A. Badolato, G. Medeiros-Ribeiro, and P. M. Petroff, *Appl. Phys. Lett.* **89**, 123124 (2006).
- ²⁴B. Alen, F. Bickel, K. Karrai, R. J. Warburton, and P. M. Petroff, *Appl. Phys. Lett.* **83**, 2235 (2003).
- ²⁵A. Högele, S. Seidl, M. Kroner, K. Karrai, R. J. Warburton, B. D. Gerardot, and P. M. Petroff, *Phys. Rev. Lett.* **93**, 217401 (2004).
- ²⁶A. Högele, B. Alen, F. Bickel, R. J. Warburton, P. M. Petroff, and K. Karrai, *Physica E (Amsterdam)* **21**, 175 (2004).
- ²⁷R. G. Newton, *Am. J. Phys.* **44**, 639 (1976).
- ²⁸A. V. Khaetskii and Y. V. Nazarov, *Phys. Rev. B* **64**, 125316 (2001).
- ²⁹S. I. Erlingsson and Y. V. Nazarov, *Phys. Rev. B* **66**, 155327 (2002).
- ³⁰P. A. Dalgarno, J. McFarlane, B. D. Gerardot, R. J. Warburton, K. Karrai, A. Badolato, and P. M. Petroff, *Appl. Phys. Lett.* **89**, 043107 (2006).
- ³¹Due to our square-wave modulation scheme, inducing a nonexponential spin decay, the conversion from the known modulation frequency to κ_{exp} rate does not need to include a factor of 2π . This has been confirmed by comparing the result of a numerical simulation using square-wave-shaped spin relaxation to the outcome of a simple rate equation model including exponential decay of spin.
- ³²C. W. Lai, P. Maletinsky, A. Badolato, and A. Imamoglu, *Phys. Rev. Lett.* **96**, 167403 (2006).
- ³³B. Eble, O. Krebs, A. Lemaitre, K. Kowalik, A. Kudelski, P. Voisin, B. Urbaszek, X. Marie, and T. Amand, *Phys. Rev. B* **74**, 081306(R) (2006).
- ³⁴As a Gedanken experiment, we assume transfer of polarization from light to nuclei via the electron spin under a static positive magnetic field. Then, due to negative electron g factor, the spin-down state has higher energy than the spin-up state. The laser is resonant with the red (first case) or the blue (second case) Zeeman transition. In the first case, electron spin is pumped to the spin-up state, which leads to nuclear spin-up polarization after an electron-nuclei flip-flop interaction. As the hyperfine constant A is positive, the energy of the electron spin-down state is consequently lowered, while the trion states remain untouched, leading to a blueshift of the red Zeeman optical transition which is being observed. The same happens in the second case, where spin-down nuclear polarization is created and the energy of the spin-up state is lowered, again leading to a blueshift of the observed transition. This scenario is clearly opposite of what we observe, thus ruling out the presence of an efficient DNSP.
- ³⁵D. V. Bulaev and D. Loss, *Phys. Rev. Lett.* **95**, 076805 (2005).
- ³⁶D. Paget, G. Lampel, B. Sapoval, and V. I. Safarov, *Phys. Rev. B* **15**, 5780 (1977).
- ³⁷P. Maletinsky, A. Badolato, and A. Imamoglu, *Phys. Rev. Lett.* **99**, 056804 (2007).
- ³⁸ $b_0^2/N = \frac{1}{3} \left(\frac{\nu_0}{8g_e\mu_B} \right)^2 \sum_i (A_i)^2 |\psi(R_i)|^4 \langle I_i^2 \rangle = \frac{1}{3N} [A^2 I(I+1)] / (g_e\mu_B)^2$; this result is obtained by assuming a boxlike confinement potential, further transforming the sum into an integral and using the localization volume of the QD electron given by $V_L^{-1} = \int d\mathbf{r} |\psi(R_i)|^4 = 8/N\nu_0$.
- ³⁹P. Maletinsky, C. W. Lai, A. Badolato, and A. Imamoglu, *Phys. Rev. B* **75**, 035409 (2007).
- ⁴⁰In this context, we note that other experiments suggest that the dynamics of the nuclear spin ensemble could be altered by the measurement itself and the hyperfine field stays locked for a time on the order of seconds (Ref. 4) [Fig. 4(b)]. In our measurements, there is some evidence of alteration of dynamics at large magnetic fields and large gate-voltage detunings (not shown in this work); however, at low magnetic fields, these locking effects do not seem to play a dominant role.
- ⁴¹T. Fujisawa, D. G. Austing, Y. Tokura, Y. Hirayama, and S. Tarucha, *Nature (London)* **419**, 278 (2002).
- ⁴²D. V. Averin and Y. V. Nazarov, *Phys. Rev. Lett.* **65**, 2446 (1990).
- ⁴³D. Goldhaber-Gordon, H. Shtrikman, D. Mahalu, D. Abusch-Magder, U. Meirav, and M. A. Kastner, *Nature (London)* **391**, 156 (1998).
- ⁴⁴S. M. Cronenwett, T. H. Oosterkamp, and L. P. Kouwenhoven, *Science* **281**, 540 (1998).
- ⁴⁵A. O. Govorov, K. Karrai, and R. J. Warburton, *Phys. Rev. B* **67**, 241307(R) (2003).

- ⁴⁶R. W. Helmes, M. Sindel, L. Borda, and J. von Delft, Phys. Rev. B **72**, 125301 (2005).
- ⁴⁷S. Seidl, M. Kroner, P. A. Dalgarno, A. Högele, J. M. Smith, M. Ediger, B. D. Gerardot, J. M. Garcia, P. M. Petroff, K. Karrai, and R. J. Warburton, Phys. Rev. B **72**, 195339 (2005).
- ⁴⁸J. M. Smith, P. A. Dalgarno, R. J. Warburton, A. O. Govorov, K. Karrai, B. D. Gerardot, and P. M. Petroff, Phys. Rev. Lett. **94**, 197402 (2005).
- ⁴⁹With Zeeman splitting $\kappa_{\uparrow\rightarrow\downarrow} \neq \kappa_{\downarrow\rightarrow\uparrow}$, i.e., the rate flipping the spin down is different from the rate flipping it up. The term $f(\varepsilon)[1 - f(\varepsilon)]$ has to be replaced by $f(\varepsilon \mp \hbar\omega_z/2)[1 - f(\varepsilon \pm \hbar\omega_z/2)]$ for $\kappa_{\downarrow\rightarrow\uparrow}$ and $\kappa_{\uparrow\rightarrow\downarrow}$, respectively.
- ⁵⁰M. I. D'yakonov, V. A. Marushchak, V. I. Perel', and A. N. Titkov, Sov. Phys. JETP **63**, 655 (1986).
- ⁵¹A. V. Khaetskii and Y. V. Nazarov, Phys. Rev. B **61**, 12639 (2000).
- ⁵²L. M. Woods, T. L. Reinecke, and Y. Lyanda-Geller, Phys. Rev. B **66**, 161318(R) (2002).
- ⁵³V. N. Golovach, A. Khaetskii, and D. Loss, Phys. Rev. Lett. **93**, 016601 (2004).
- ⁵⁴D. V. Bulaev and D. Loss, Phys. Rev. B **71**, 205324 (2005).
- ⁵⁵R. J. Warburton, C. Schaflein, D. Haft, F. Bickel, A. Lorke, K. Karrai, J. M. Garcia, W. Schoenfeld, and P. M. Petroff, Nature (London) **405**, 926 (2000).
- ⁵⁶Y. Yamamoto and A. Imamoglu, *Mesoscopic Quantum Optics* (Wiley, New York, 1999).
- ⁵⁷Including Zeeman splitting, relation (A6) can be written in the form $\kappa_{\uparrow\rightarrow\downarrow} = \exp(-\hbar\omega_z/2kT) \int_{\varepsilon} d\varepsilon A(\varepsilon) \tilde{f}(\varepsilon)$ and, similarly, $\kappa_{\downarrow\rightarrow\uparrow} = \exp(\hbar\omega_z/2kT) \int_{\varepsilon} d\varepsilon A(\varepsilon) \tilde{f}(\varepsilon)$, with $\tilde{f}(\varepsilon) = [1 + \exp[\varepsilon + (\hbar\omega_z/2kT)]] [1 + \exp[\varepsilon - (\hbar\omega_z/2kT)]]^{-1}$. In Eq. (C1), the $\kappa\bar{n}$ term has to be replaced by $\kappa_{\uparrow\rightarrow\downarrow}$, whereas the $\kappa(\bar{n}+1)$ is replaced by $\kappa_{\downarrow\rightarrow\uparrow}$. As a consequence, the ratio of spin-up versus spin-down state occupation is governed, as one would expect, by the Boltzmann factor $\kappa_{\uparrow\rightarrow\downarrow}/\kappa_{\downarrow\rightarrow\uparrow} = \exp(-\hbar\omega_z/kT)$.